Thermal transport across high-pressure semiconductor-metal transition in Si and $Si_{0.991}Ge_{0.009}$

Gregory T. Hohensee*
Department of Physics, Materials Research Laboratory, University of Illinois at Urbana-Champaign, Urbana, Illinois 61801, USA

Michael R. Fellinger, Dallas R. Trinkle, and David G. Cahill
Department of Materials Science and Engineering, Materials Research Laboratory, University of Illinois at Urbana-Champaign, Urbana, Illinois 61801, USA

(Received 17 February 2015; revised manuscript received 14 April 2015; published 7 May 2015)

Time-domain thermoreflectance (TDTR) can be applied to metallic samples at high pressures in the diamond anvil cell and provide noncontact measurements of thermal transport properties. We have performed regular and beam-offset TDTR to establish the thermal conductivities of Si and $Si_{0.991}Ge_{0.009}$ across the semiconductor-metal phase transition and up to 45 GPa. The thermal conductivities of metallic Si and Si(Ge) are comparable to aluminum and indicative of predominantly electronic heat carriers. Metallic Si and Si(Ge) have an anisotropy of approximately 1.4, similar to that of beryllium, due to the primitive hexagonal crystal structure. We used the Wiedemann-Franz law to derive the associated electrical resistivity, and found it consistent with the Bloch-Grüneisen model.

DOI: 10.1103/PhysRevB.91.205104 PACS number(s): 44.10.+i, 65.40.−b, 72.15.Eb, 63.20.dk

I. INTRODUCTION

High-pressure thermal transport measurements can provide information and reveal physics that is not otherwise clear from ambient-pressure experiments. Geophysical models of planetary heat flow, notably near the Earth's core-mantle boundary where the pressure reaches 130 GPa, rely on knowledge of the thermal conductivity of minerals at high temperatures and pressures [1,2]. Experimental data on the pressure scaling of thermal transport in amorphous [3] and crystalline materials [2,4–10] helps build a basis for extrapolation to more extreme pressure-temperature conditions.

Similarly, high-pressure electrical transport experiments have been invaluable in the study of the physics of superconductors, as they enable monitoring of superconductivity as a function of atomic spacing and phase transitions under compression [11,12]. The broad interest in carbon materials also extends to electrical transport measurements at high pressure [13], and metal-insulator transitions under pressure in silicon [14], CS_2 [15,16], MoS_2 [17,18], and VO_2-related materials [19,20], among others [21], have received a great deal of attention recently.

Silicon is an extensively studied material, as a template for other materials and in its own right for its nanoscale thermal transport dynamics [22–26]. Silicon also has several phase transitions at moderately high pressures: from diamond cubic to β-Sn above 11 GPa, to primitive hexagonal near 15 GPa, and to hcp through an intermediate *Cmca* phase around 36–42 GPa [27–29]. In 1962 Minomura and Drickamer observed an abrupt, five to six orders of magnitude drop in two-point electrical resistance in silicon above 20 GPa, concluding that it had entered a metallic phase [30]. Since then, experiments have used the resistance drop to map out the semiconductor-metallic phase transition, either as a function of temperature [31] or as a function of uniaxial pressure by local indentation of silicon along different crystalline axes [32]. The superconducting phase transition for metallic Si under pressure has also been mapped out as a function of pressure by electrical transport measurements [33]. Si also shows a pronounced change in optical reflectivity into the metallic phase [34]. Despite this attention, we are not aware of any absolute electrical resistivity or thermal conductivity reports for metallic silicon.

While there are a variety of techniques sensitive to the onset of a metallic phase under pressure, absolute thermal and electrical transport measurements often rely on physical contact with the sample, such as the Angstrom method [4] or four-point probe. The requisite metal leads must be simultaneously protected from the high-pressure environment, electrically insulated from the gasket, and in good contact with the sample. Stress gradients can build under pressure to damage or deform the metal leads, and the sample geometry will also change under compression or across phase transitions [35]. For experiments in the highest pressure ranges where the diamond anvil cell (DAC) is necessary [36], researchers have developed designer diamond anvils with embedded metal leads to perform electrical measurements in the DAC [37,38].

Recently, all-optical techniques have been developed for thermal transport measurements at high pressure in the DAC. Optical techniques are less demanding in that the diamond anvils double as optical windows. For simultaneous high-pressure, high-temperature measurements in particular, high-speed spectroradiometry is used to sample blackbody radiation from intensely laser-heated DAC samples. The resulting 2D temperature map is then fitted for thermal conductivity [39–41]. Optical laser flash diffusivity experiments have also measured the thermal diffusivity of a variety of materials under pressure, including MgO, $MgSiO_3$, and Fe-doped variants [2,8,9].

Our approach has been to leverage time-domain thermoreflectance (TDTR), an established ultrafast pump-probe technique for measuring thermal transport properties [42–44]. Over the past few years high-pressure TDTR experiments have provided new insight into the role of weak interface bonding in suppressing the thermal conductance of an interface between two materials [45], as well as information about

*Corresponding author: hohense2@illinois.edu

 ©2015 American Physical Society

the mechanisms behind the enhanced heat conduction at interfaces between dissimilar materials [46]. TDTR has also verified theoretical predictions of the thermal conductivity in amorphous and crystalline solids at high pressure [3,7,10].

In this paper, we report thermal conductivity measurements of [001] Si and the mixed crystal $Si_{0.991}Ge_{0.009}$ up to 45 GPa. This spans multiple phase transitions, in particular the semiconductor-metal transition which abruptly alters the thermal transport. We then apply the Wiedemann-Franz law to derive the anisotropic electrical resistivity of the metallic phase.

II. EXPERIMENTAL METHOD

For measurements of thermal conductivity by TDTR, the sample is typically coated with an approximately 80 nm metal transducer film, the pump pulses heat the surface, and the probe pulses monitor the change in reflectance over time due to the temperature rise and subsequent cooling. A thermal model for the TDTR signal is generated from a solution to the heat diffusion equation for a multilayered sample, where each layer is assigned a thickness, heat capacity, and thermal conductivity [42]. The thermal model is fitted to the TDTR signal by varying one or two unknown thermal parameters, for example the thermal conductivity Λ of a bulk isotropic substrate, and the interface thermal conductance G between the metal transducer and the sample.

We performed TDTR measurements on Al-coated and Au(Pd)-coated commercial undoped Si and Si(Ge) wafers, where the Pd and Ge contents were established by Rutherford backscattering spectroscopy to be 5% and 0.9%, respectively. The Al and Au(Pd) thin films were deposited by dc magnetron sputtering, with thicknesses of approximately 80 nm confirmed by picosecond acoustics [47]. We also performed TDTR measurements on bare metallic Si and Si(Ge) in the primitive hexagonal phase at high pressures, and supplemented these measurements with beam-offset TDTR as well.

For a sample coated with a metal transducer layer, the sensitivity of the TDTR measurement to the cross-plane thermal conductivity Λ_z comes from the out-of-phase temperature response of the transducer surface relative to the pump heating at the pump modulation frequency f. This phase lag depends on the areal heat capacity of the transducer relative to the volumetric heat capacity C of the substrate integrated over the thermal penetration depth $L_{\text{th}} = \sqrt{\Lambda_z/(\pi C f)}$. Hence conventional TDTR with a transducer layer is sensitive to the thermal effusivity, since $L_{\text{th}} C \propto \sqrt{\Lambda_z C}$.

If TDTR is used to measure a bulk metallic sample without a transducer layer, the measurement loses almost all sensitivity to the Λ_z of the substrate. However, with or without a transducer, for sufficiently small pump and probe laser spot sizes on the sample, the heat transport is no longer in the one-dimensional limit and the TDTR measurement gains sensitivity to thermal diffusion in the plane of the sample. For an uncoated bulk metallic substrate, TDTR mainly probes the in-plane thermal diffusion length relative to the pump and probe laser spot sizes. As such, for sufficiently low pump modulation frequency and small pump and probe spot sizes, TDTR is sensitive to the in-plane thermal diffusivity of a bulk metallic sample. In fact, since the areal heat capacity of a metal transducer layer is a major source of systematic uncertainty in conventional TDTR, measurements on an uncoated bulk metal can be even more precise, assuming the laser spot size is also measured precisely.

Our thermal model for metallic samples assumes that heat is initially deposited in the electrons within an optical penetration depth, that the electrons and phonons equilibrate over some electron-phonon thermalization length, and that the thermal penetration depth at our pump modulation frequency is much longer than either of these lengths. We can calculate the optical penetration depth in metallic Si because Hanfland *et al.* [34] have measured the diamond/silicon reflectance R and calculated the imaginary part of the silicon permittivity ϵ_2 at high pressures. At our center wavelength of 785 nm, they report $R \approx 0.7$ and $\epsilon_2 \approx 15$ at 30 GPa. Since the optical properties of diamond are comparatively insensitive to pressure, this gives us enough information to back out the refractive index n and absorption coefficient κ for metallic silicon. We find that $n \approx 1.4$ and $\kappa \approx 5.5$ at this wavelength and pressure, for an optical penetration depth of $\alpha^{-1} \approx 11$ nm.

The electron-phonon thermalization length in metals is typically 10–100 nm, depending on electron-phonon coupling strength. We estimate the relevance of electron-phonon dynamics for TDTR measurement of bare metallic Si by specifying in the model that energy deposition is uniform and immediate in the top L_{ep} nanometers of the sample. As for any other model parameter, we can calculate the sensitivity of the TDTR signal to L_{ep} as a function of delay time. Taking an extreme case where $L_{\text{ep}} \approx 100$ nm as in Au, and using representative model parameters for metallic Si, we computed sensitivities and found that the TDTR signal is five times less sensitive to L_{ep} than to the thermal conductivity Λ at 500 ps, and ten times less at 1 ns delay time. From our experimental data, the thermal penetration depth in metallic Si is already $\approx$270 nm or longer after 1 ns. By this reasoning we find that we can fit the TDTR signal for Λ starting from 1 ns delay time, without quantitative knowledge of the electron-phonon coupling in the material.

We paired each TDTR measurement on bare metallic Si and Si(Ge) with a beam-offset TDTR measurement at the same position on the sample. Beam-offset TDTR is a variation of TDTR where the pump beam spot is scanned across the probe spot at a fixed delay time, typically along the two lateral axes in the plane of the sample surface [48]. Taken at short positive delay time, the $V(\text{in})$ signal of beam-offset TDTR provides a precise measure of the correlated pump and probe spot sizes, before heat has time to spread in the sample. We then take two perpendicular beam offset scans in the plane of the sample at short negative time delay, obtaining two $V(\text{out})$ profiles. The width of each $V(\text{out})$ beam offset profile is determined by the initial spot size and the thermal penetration depth along that direction in the plane of the sample.

Because the TDTR pump modulation is in the MHz frequency range, even high thermal conductivity samples thin enough for DAC loading are essentially bulk or semi-infinite for the thermal model. At 1 MHz, a sample with a thermal conductivity of 200 W m^{-1} K^{-1} and a heat capacity

on the order of 2 J cm^{-3} K^{-1} has a thermal penetration depth $L_{th} = \sqrt{\Lambda/(\pi C f)} \approx 5.6$ μm, much less than the 10–15 μm thickness of typical DAC samples. In our experiments on Si and $Si_{0.991}Ge_{0.009}$, the lowest modulation frequency was 3.35 MHz, L_{th} was always less than 4 μm, and the sample thicknesses between 8–16 μm. Therefore, because we measure the side of the sample facing the silicone oil pressure medium, the exact thickness of the sample and the thermal properties of the diamond anvil are irrelevant to our measurement.

For the bare metallic Si and Si(Ge) data sets, we used a 3.35 MHz pump modulation frequency and a laser spot size of approximately 3 μm e^{-2} radius, which we measured at each pressure point. The resulting signal-to-noise and significant lateral diffusion length relative to the spot size permitted beam-offset TDTR fits to the thermal diffusivity to within 10%. The only other relevant parameter in the thermal model is the thermal effusivity of the silicone oil pressure medium in the DAC, which is comparatively negligible. For conventional TDTR on Al- or Au(Pd)-coated Si and Si(Ge), systematic uncertainty in the transducer areal heat capacity yields the usual 5%–10% uncertainty in the fitted thermal conductivities for a given Si heat capacity.

Since TDTR has previously been used to measure the dynamic heat capacity across the metal-insulator transition (MIT) in vanadium dioxide (VO_2) [49], it is worthwhile to consider whether our present TDTR experiment is sensitive to the dynamic heat capacity across the various high-pressure silicon phase transitions at room temperature. Deb *et al.* [50] studied pressure-induced amorphization of porous silicon, and also provided a calculated pressure-temperature phase diagram for crystalline Si. In their Fig. 3(a), they portray the diamond cubic to β-Sn phase boundary as having a slope of 10^3 K per GPa, extending up to a melting temperature above 900 K. We do not expect the few-K temperature excursions in our experiment to create significant thermal pressure or cross a phase boundary in temperature.

In TDTR, one can obtain sensitivity to the dynamic heat capacity of a phase transition if the transition rate exceeds the time scale of the TDTR pump modulation frequency. In our experiment, the pump modulation time scale is $\tau \approx (2\pi f)^{-1} \approx 16$ ns. The TDTR study of the MIT of VO_2 [49] had sensitivity because the VO_2 transition is subpicosecond, which is what makes it interesting for ultrafast optical switching [51]. In silicon, all the pressure transitions at room temperature involve changes in symmetry and atomic bonding; it is not obvious that they would have nanosecond transition rates, even if we were near a temperature phase boundary.

Experimentally, the DAC pressure gradient that we describe in Sec. III allowed us to avoid taking measurements on Si within 1 GPa of any phase transition. The small pressure gradient across our samples meant that we could observe the wave front of a phase transition between higher and lower pressure regions of the samples. These could be seen in visible light by increased optical reflectivity in the metallic phases, as well as volume collapse across the transitions. We always applied an $\approx$1 GPa pressure increment after observing such a wave front, so that the measurement was not taken near a phase boundary.

III. DAC SAMPLE PREPARATION AND PRESSURE CALIBRATION

We used commercial [001] Si [P-type (boron), 3–50 Ω cm resistivity] and $Si_{0.991}Ge_{0.009}$ wafers for our experiment. For the samples measured with a metal film transducer, the Al and $Au_{0.95}Pd_{0.05}$ films were deposited by dc magnetron sputtering. The Si and Si(Ge) substrates were heated to approximately 600 °C for 30 minutes in vacuum and allowed to cool immediately before Al and Au(Pd) deposition in the same chamber, without exposure to air. We deposited Au(Pd) instead of pure Au because Au(Pd) yields a clear picosecond acoustic signal from which we can extract the Au(Pd) film thickness *in situ*, unlike Au [52]. After sputtering, the Si and Si(Ge) samples were back-polished to 8–16 μm thickness, and squares approximately 100 μm × 100 μm in size were cleaved and loaded into the DAC with a low-viscosity silicone oil (1 cSt octamethyltrisiloxane, molecular weight 237) as the pressure-transmitting medium [53]. The bare Si and Si(Ge) samples were back-polished and loaded into the DAC without heating or sputter deposition.

One to three ruby spheres were included in the DAC sample chamber for pressure calibration by ruby fluorescence [54]. The ruby fluorescence shift can be sensitive to nonhydrostatic behavior of the pressure medium, but the range of variations is small below 50 GPa [55]. We estimate ±0.5 GPa uncertainty in the ruby pressure from spectrometer resolution [56].

An important aspect of using ruby as a pressure calibrant is that the pressure experienced by the ruby is not necessarily the pressure at the region of the sample measured by TDTR. For a quasihydrostatic medium like silicone oil, pressure gradients on the order of 10% can develop across the sample chamber [57]. It is difficult to ensure that the spatial separation between ruby and sample is small after loading a fluid medium, and the gasket hole that forms the sample chamber can also drift with increasing pressure. As a result the ruby can be at lower pressure near the edge of the diamond culet, while the sample remains at the culet center under slightly higher pressure.

Because TDTR also provides an *in situ* Brillouin frequency measurement of the pressure medium [3], it is possible to calibrate the medium's Brillouin frequency versus pressure, and later compare the measured Brillouin frequency against the pressure reading from a distant ruby. We have recently done this for silicone oil [46], and in Fig. 1 we make that comparison for DAC loadings with the bare Si and Si(Ge) samples. Above 15 GPa the pressure at the sample deviated from the ruby pressure by approximately 15% (Fig. 1, dashed green line), plus or minus 1 GPa (solid green lines). We can extract the raw Brillouin frequencies from our TDTR signals to within 2%, but systematic error in our frequency-to-pressure calibration is expected to be somewhat larger, between 5% and 10%. More data points from adjacent ruby and TDTR measurements under pressure are needed for a more precise silicone oil Brillouin frequency calibration, but even so we are able to correct for significant differences between ruby and sample pressures in this manner.

To judge whether this observed gradient is realistic, we examine literature data for the ruby R_1 linewidth as a function of pressure in silicone oil pressure media. Increases in R_1

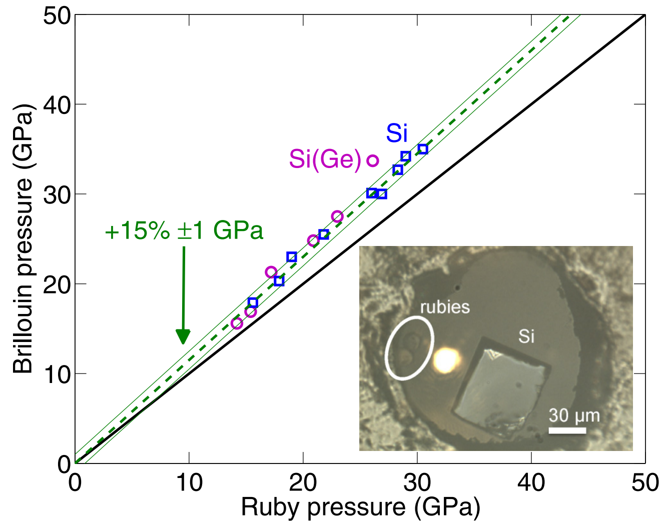

FIG. 1. (Color online) Observed pressure differential between ruby and samples. Our TDTR signals contain normal-incidence Brillouin frequency data from the pressure medium, and in prior work we have calibrated these frequencies in 1 cSt silicone oil against the ruby pressure standard [46]. We observed that when the ruby is displaced relatively far from the Si or Si(Ge) sample, the pressure gradient in the quasihydrostatic pressure medium caused the ruby and sample pressures to differ significantly. The black solid line is for 1:1 agreement between ruby pressure and the pressure at the sample. The green dashed line marks sample pressures that are 15% higher than the pressure at the ruby, and the green solid lines are ±1 GPa above and below the +15% line. The inset photo shows a view into the DAC sample chamber, when this bare Si piece was on the cusp of the β-Sn transition. The sample was centered on the 400 μm diameter anvil culet, and the pressures at the sample were consistently $\approx$15% higher than the ruby pressure.

linewidth with pressure correlate with decreased hydrostaticity in the pressure medium. Previous work with silicone oil pressure media indicate that a 10% standard deviation or gradient in pressure across a DAC sample chamber is not unusual above 20 GPa [53,57]. The maximum deviation from center to edge of a sample chamber that has drifted under pressure, then, is likely to be comparable to the 15% that we report in Fig. 1 for some of our DAC loadings.

IV. PRESSURE-DEPENDENT THERMAL MODELING

As in most TDTR experiments our thermal model is simply an analytic solution to the heat diffusion equation through a multilayer, as laid out for coaligned pump and probe beams by Cahill in 2004 [42]. All high-pressure TDTR experiments must additionally consider bidirectional heat flow from the heated sample surface [58], both into the sample and into the pressure medium, which is in this case silicone oil. Since very few thermal properties have been experimentally measured at high pressure, we must calculate most of these properties as accurately as possible, leaving the most complex properties such as thermal conductivity to be fitted by our experimental data.

We model the pressure-dependent thermal properties of the metal transducer films of Al and Au(Pd) in the same manner as in our previous work [46]. Since we can only measure the thermal diffusivity or effusivity of silicon, all of our reported silicon thermal conductivity data are necessarily dependent on the accuracy with which we calculate the silicon heat capacity under pressure. Since our model includes heat transport in the silicone oil pressure medium, we must also consider how sensitive our measurement is to that heat transfer pathway, and provide an adequate estimation for the silicone oil thermal conductivity and heat capacity under pressure.

First, we perform *ab initio* lattice dynamics calculations for Si in the diamond cubic, primitive hexagonal, and hcp phases at high pressure due to the absence of experimental heat capacity data. Density functional theory (DFT) computes forces on displaced atoms for input to the direct force-constant approach to phonon thermodynamics [59,60]. The DFT calculations utilize the plane-wave basis program VASP [61]. The Perdew-Burke-Ernzerhof generalized gradient approximation functional [62] accounts for electron exchange and correlation, and a projector augmented wave potential [63] with electronic configuration [Ne]$3s^2 3p^6$ generated by Kresse and Joubert [64] represents the Si nuclei and core electrons. Forces on atoms displaced from their ideal lattice sites by 0.02 Å determine the force constants for Si in the diamond cubic phase at 11 GPa (DFT lattice parameter $a = 5.289$ Å), the primitive hexagonal phase at 15, 27, and 38 GPa (DFT lattice parameters $a = 2.549$ Å and $c = 2.402$ Å, $a = 2.494$ Å and $c = 2.360$ Å, and $a = 2.452$ Å and $c = 2.239$ Å, respectively), and the hcp phase at 42 GPa (DFT lattice parameters $a = 2.467$ Å and $c = 4.182$ Å). The diamond cubic and primitive hexagonal calculations require a plane-wave energy cutoff of 400 eV, and the energy cutoff for the hcp calculation requires 450 eV. Force calculations are carried out in a 4×4×4 supercell for diamond cubic (128 atoms), 5×5×5 supercells for primitive hexagonal (125 atoms), and a 5×5×3 supercell for hcp (150 atoms). The corresponding k-point meshes for each supercell are 4×4×4, 6×6×6, and 6×6×6. For the insulating diamond cubic phase at 11 GPa we use the linear tetrahedron method [65,66] with Blöchl corrections [67] for the Brillouin zone integration,

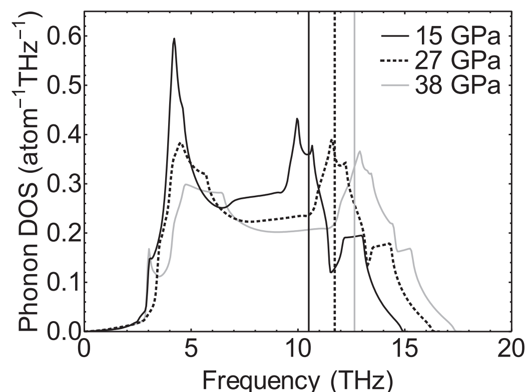

FIG. 2. Phonon density of states (DOS) for primitive hexagonal Si at high pressure. Density functional theory computes the phonon DOS at 15, 27, and 38 GPa. The DOS broadens with pressure, causing an increase in the Debye frequency which is computed from the first frequency moment of the DOS [88]. The Debye frequencies shown as vertical lines determine Debye temperatures Θ for the Bloch-Grüneisen model of electrical resistivity.

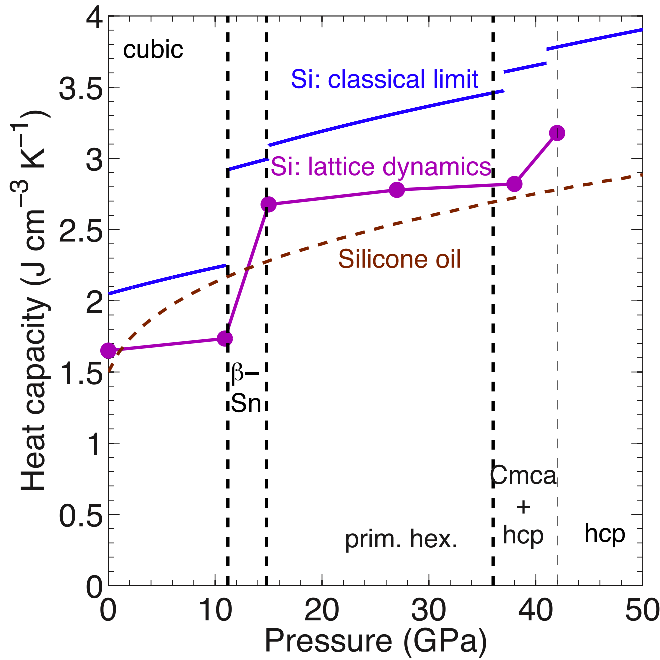

FIG. 3. (Color online) Computed Si and silicone oil heat capacities. The Si heat capacity (magenta points and interpolation line) used to extract the thermal conductivity Λ from our TDTR data is computed using the phonon densities of states from density functional theory (Fig. 2). The point at 38 GPa in the mixed-phase (*Cmca* + hcp) region is computed for the primitive hexagonal structure. By comparing the classical limit $C = 3Nk_B$ for Si (blue lines) to our computation, we see that most of the change in heat capacity is driven by the change in density. The heat capacity for silicone oil (dashed brown line) is extrapolated on the assumption that the heat capacity per molecule is constant, so that the only pressure dependence is from changes in density.

while for the metallic primitive hexagonal and hcp phases, we use order-one Methfessel-Paxton smearing [68] with energy smearing widths of 0.6 eV (hexagonal) and 0.5 eV (hcp). These settings ensure energy convergence of less than 1 meV/atom for each phase. Figure 2 shows the computed phonon density of states (DOS) for the primitive hexagonal phase at 15, 27, and 38 GPa.

Figure 3 plots the calculated $C(P)$ for Si and the silicone oil pressure medium. The *ab initio* Si heat capacity was calculated at six pressures (magenta points), and for the thermal model we simply use a linear interpolation between these points (magenta line) for the Si heat capacity at all pressures. As can be seen by comparing the *ab initio* curve against the classical (high temperature) $C = 3Nk_B$ limit (black lines), the jumps in heat capacity across the phase transitions are largely density driven. Our use of interpolation rather than direct calculation for the β-Sn heat capacity may underestimate the heat capacity in that phase, following the behavior of the classical limit. This would mean we are overestimating the cross-plane Λ_z from our transducer-coated samples.

For silicone oil, we extrapolated $C(P)$ assuming that the silicone oil heat capacity per molecule is constant with pressure, and that the volumetric heat capacity is solely a function of density. We derived the change in density with pressure in our previous work from the Lorentz-Lorenz relation and a pressure-volume equation of state (EOS) fitted to our own Brillouin frequency versus pressure data [46].

We have previously extrapolated the silicone oil thermal conductivity $\Lambda(P)$ from low-pressure data [69] using the minimum thermal conductivity model, with the assumption that the ratio of the longitudinal and transverse speeds of sound is constant with pressure [46]. This assumption has been previously used to successfully replicate the pressure dependence of PMMA [3].

For conventional TDTR, the sensitivity to the silicone oil relative to the Si and Si(Ge) samples is approximately the ratio of their thermal effusivities $\sqrt{\Lambda C}$. Our calculations in Ref. [46] showed that the silicone oil thermal conductivity remains of order 1 W m^{-1} K to 50 GPa. Since the thermal conductivity of both Si and Si(Ge) are 1–2 orders of magnitude larger than that of silicone oil, and the Si and Si(Ge) heat capacities are larger than that of silicone oil, our measurements are 10 to 100 times more sensitive to the Si and Si(Ge) effusivity than to the silicone oil effusivity. The same argument holds for the bare Si and Si(Ge) measurements, for which the measured parameter is thermal diffusivity rather than effusivity.

V. INTERFACE THERMAL CONDUCTANCE

Figure 4 shows the measured interface thermal conductances between the Al and Au(Pd) transducers and their Si and Si(Ge) substrates. Blue symbols represent data for Al/Si interfaces, while open and closed brown symbols are

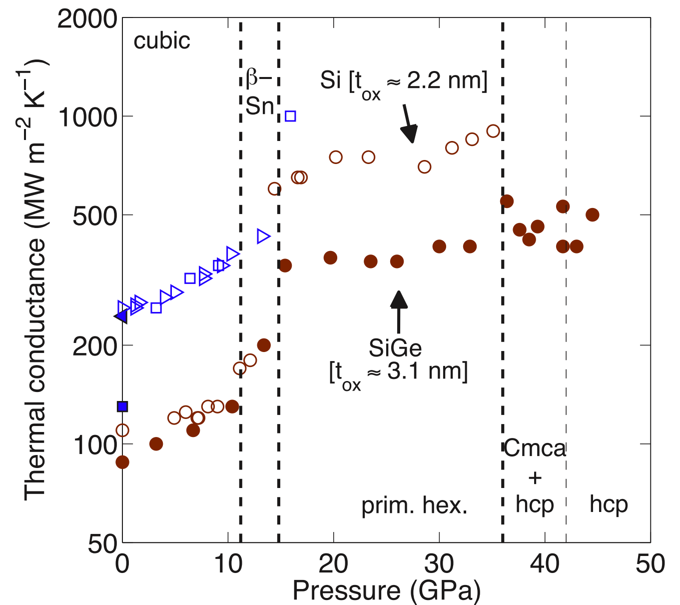

FIG. 4. (Color online) Si and Si(Ge) interface thermal conductances. Blue symbols represent data for interfaces between Al and Si with ≈2.2 nm native oxide, determined by ellipsometry. Open and closed brown symbols are for Au(Pd)/Si and Au(Pd)/Si(Ge) interfaces with ≈2.2 and ≈3.1 nm native oxide, respectively. The Al/Si data showed signs of hot electron transport into the metallic Si substrate, indicating direct metal-metal contact over some fraction of the interfacial surface area. This invalidated our thermal model, so our Al/Si data stop as Si becomes metallic.

for Au(Pd)/Si and Au(Pd)/Si(Ge) interfaces, respectively. It is important to note that all of the Si and Si(Ge) samples have a native oxide of 2–3 nm on their surface, so the Al/Si, Au(Pd)/Si, and Au(Pd)/Si(Ge) interface conductances all include the thermal resistance of the native oxide. We measured the native oxide thicknesses on untreated Si and Si(Ge) wafers by ellipsometry, obtaining approximately 2.2 and 3.1 nm, respectively.

The difference in initial thermal conductances between Au(Pd)/Si and Au(Pd)/Si(Ge) is likely due to weak interfacial bonding in the latter sample, although both were heated to approximately 600 °C in vacuum prior to Au(Pd) deposition. The difference is suppressed by 10 GPa, as expected from prior work on weakly bonded Al/SiC interfaces under pressure [45]. Meanwhile the Al/Si sample conductance is high and reversible up to 13 GPa (open and filled blue triangles), just before the β-Sn to primitive hexagonal phase transition. The initial Al/native oxide/Si conductance is typical of a clean interface on Si with native oxide, so we expect the pressure dependence is intrinsic to Al/native oxide/Si interfaces with $\approx$2 nm of native SiO_2. The Al/native oxide/Si thermal conductance increases from 260 to 380 MW m^{-2} K between 0 and 10 GPa, a nearly 50% increase.

We can use the radiation limit for Al to estimate the maximum possible increase in thermal conductance due to elastic phonon processes [46]. In the radiation limit picture, the $\approx$20% increase in Al phonon cutoff frequency with pressure [46] would suggest an $\approx$75% increase in thermal conductance. As this limit is larger than the observed increase, elastic processes can explain the increase in Al/native oxide/Si interface conductance that we observe under pressure. This is consistent with recent theoretical work [70].

We can also compare the observed increase in interface conductance to the change in the theoretical maximum conductance G_{max} for Al, which is defined as the interface conductance assuming 100% transmission of all Al phonon modes incident on the interface [71]. Figure 4 of Ref. [71] plots G_{max} for Al as a function of pressure up to 60 GPa, and predicts an $\approx$6% increase in G_{max} for Al between 0 and 10 GPa, much smaller than the nearly 50% increase in G that we observe for Al/native oxide/Si. The authors of Ref. [71] made a similar observation when comparing G_{max} for Al against the G of an Al/MgO interface between 0 and 10 GPa. We make the same inference as they made: that interfacial stiffness is an influential parameter for interfacial conductance, even when the interface is relatively clean.

We did not remove the Si and Si(Ge) native oxides prior to Al or Au(Pd) deposition because we were interested in how the thermal conductance of phonons might change across the semiconductor-metal transition starting near 15 GPa. We observed the following changes in the Al/native oxide/Si interface thermal conductance as we increased the pressure into the metallic Si phase. First, the hot-electron peak in the picosecond acoustics disappeared when Si became metallic, and returned on decompression back to nonmetallic Si [47]. Hot electrons from a pump pulse cause a hot-electron peak in the TDTR signal by generating a stress discontinuity at the interface between the transducer and an electrically insulating surface, such as an oxide layer or a nonmetallic substrate. Second, the decay rate of the in-phase TDTR signal, which determines the apparent interface thermal conductance, increased sharply after Si became metallic. Fits to the interface conductance G yielded values of 1–3 GW m^{-2} K^{-1}, at the upper limit of the TDTR measurement sensitivity to G. These values are 10% of what is typical for electronic thermal transport between two metals at ambient pressure. The fitted G was also not reversible on decompression to ambient pressure. An Al/native oxide/Si sample compressed to just below the metallic transition returned to about 260 MW m^{-2} K^{-1} conductance, whereas decompression from the metallic phase yielded 500 MW m^{-2} K^{-1} at ambient, similar to the interface conductance between Al and a Si wafer that was HF dipped to remove the native oxide. These results are suggestive of direct metal-metal contact between Al and Si after Si becomes metallic. We do not know how this comes about. One possibility may be the mechanics of the phase transition, another may be chemistry between the Al and native oxide.

We have chosen not to include the Al/Si TDTR results for metallic Si for two reasons. First, the TDTR measurement lacks significant sensitivity to interface conductances on the order of a GW m^{-2} K^{-1}. Second, our thermal model predicted thermal conductivities for metallic Si from the Al/Si data that were far in excess of the values we obtained from our Au(Pd)/Si and our bare metallic Si data, which were consistent with one another. An assumption of our thermal model is that heat is initially deposited only in the transducer layer; if there is appreciable direct metal-metal contact at the interface, energy from hot electrons may deposit directly in the substrate, which violates that assumption. Conversely, we do include the Au(Pd)/Si and Au(Pd)/Si(Ge) results because the interface thermal conductances were measurable, and the obtained thermal conductivities were consistent with the results from the bare metallic Si TDTR data, for which interfacial transport is a nonissue. We do not know why the Au(Pd) results were consistent with bare metallic Si and the Al results were not. It could possibly have to do with differences in the mechanical properties or chemical reactivities of Al versus Au(Pd) at high pressures.

After the semiconductor-metal transition, the thermal conductances for Au(Pd) on Si and Si(Ge) have average values of 750 and 470 MW m^{-2} K^{-1}, respectively. The ratios of the oxide thicknesses and interfacial thermal resistances were both approximately 1.6. The interfacial conductances were equivalent to the thermal resistance of oxides with a thermal conductivity of approximately $\approx$1.5 MW m^{-2} K^{-1} and initial thicknesses given in Fig. 4. We note that the interface conductances between Au(Pd) and metallic Si and Si(Ge) are of a similar magnitude to the electron-phonon conductance for Au that we extrapolated to high pressure in our previous work [46], which would act as a limiting interface conductance if the Au electrons cannot propagate or deposit energy into the substrate [46,72].

VI. THERMAL CONDUCTIVITY—SEMICONDUCTING

Figure 5(a) shows the measured thermal conductivities for the Al- and Au(Pd)-coated Si and Si(Ge) samples, by conventional TDTR. Blue squares and triangles are Al/Si data, open and closed brown circles are Au(Pd) on Si and Si(Ge),

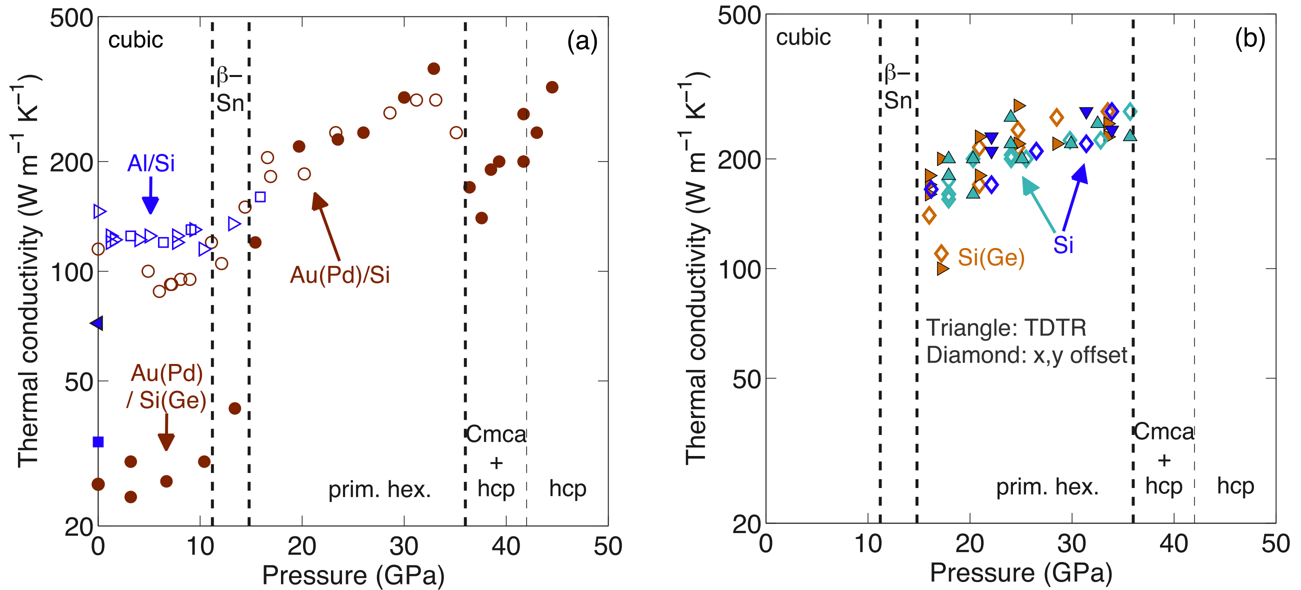

FIG. 5. (Color online) Si and Si(Ge) thermal conductivities Λ. Panel (a) shows Λ extracted from the thermal effusivity versus pressure measured by TDTR on Al- and Au(Pd)-coated samples, and panel (b) shows Λ from conventional and beam-offset TDTR on uncoated metallic Si and Si(Ge) samples. In panel (a), the blue squares and triangles are from Al-coated Si, and the brown open and filled circles are from Au(Pd)-coated Si and Si(Ge), respectively. The vertical lines denote phase transition pressures. In panel (b), the cyan and orange triangles are TDTR measurements on bare metallic Si and Si(Ge), respectively. The corresponding pairs of beam-offset measurements for each TDTR point are represented by cyan and orange diamonds. Blue symbols are decompression (decreasing pressure) data from the bare metallic Si sample. The equivalence between Si and Si(Ge) Λ in the metallic primitive hexagonal phase suggests that the phonon contribution to Λ, which we expect to be different in Si versus Si(Ge), is negligible. All of the metallic Si and Si(Ge) thermal conductivities are confined to a band of values, indicating that this hexagonal phase is both polycrystalline and anisotropic in its thermal transport.

respectively. The filled blue square and triangle at 0 GPa are the thermal conductivities of the recovered Al/Si sample after decompression from the β-Sn and primitive hexagonal phases near 13 and 16 GPa, respectively. Vertical lines mark phase transition pressures [27–29].

The thermal conductivity of amorphous [3] and crystalline materials [10] will generally increase with pressure due to bond stiffening. In a crystal the pressure scaling is stronger due to the reduction in the phonon density of states and associated reduction in the rate of three-phonon scattering. The thermal conductivity is expected to scale with powers of the bulk modulus K_{T}, specifically $K_{\mathrm{T}}^{1/2}$, $K_{\mathrm{T}}^{3/2}$, and K_{T} for amorphous, crystalline, and mixed crystalline materials. The Si(Ge) data in the diamond cubic phase are not inconsistent with this expectation, although they are also consistent with no pressure scaling. The diamond cubic Si thermal conductivity, however, is lower than its zero pressure value and constant in the diamond cubic phase.

At ambient pressure, the diamond cubic phase of Si is known to exhibit non-Fourier thermal transport when heated at sufficiently small length scales [23–25]. In particular, Wilson and Cahill measured an approximately 15% reduction in the apparent thermal conductivity of bulk Si by conventional TDTR as the laser spot size is decreased from 10 to 3 μm e^{-2} radius due to nondiffusive transport [25]. We performed spot-size-dependent measurements down to 3 μm spot size on Al/Si samples across the entire diamond cubic high-pressure phase. We obtained an expected 146 W/m K at 0 GPa for the largest spot size, but above 1 GPa, we measured conductivities of 115–130 W m^{-1} K^{-1} for all spot sizes with no discernible pressure or spot-size dependence. As such we distinguished symbols [blue open triangles and squares, Fig. 4(a)] for different samples, but not different spot sizes. The scatter in our current high-pressure data is comparable to the spot-size dependence in ambient Si down to a 3 μm spot size. It is conceivable that a more precise series of measurements down to a 1 μm spot size could resolve a trend.

The lack of pressure dependence that we observe in the thermal conductivity of the diamond-cubic phase of Si is unusual: more typical behavior can be seen in diamond, which has the same crystal structure and is predicted to have an increasing trend in its thermal conductivity under pressure [73]. A recent first-principles calculation by Parrish *et al.* for Si up to $\pm 3\%$ strain (equivalent to $\approx$4 GPa for Si) reports a similar lack of pressure dependence in the thermal conductivity of compressed Si [74]. Parrish *et al.* observed that Si atoms had shorter phonon lifetimes and were allowed greater root-mean-square (rms) displacement under compression. Along the same lines, Soma [75] and Shen *et al.* [76] have produced theoretical and experimental work indicating that the transverse acoustic modes in diamond cubic Si soften as the pressure approaches the β-Sn phase transition. This is in contrast to the behavior of diamond, as Broido *et al.* calculated no significant alteration in the transverse acoustic modes of diamond up to 400 GPa [73]. Softening of the transverse phonons in silicon increases their occupation number and increases their umklapp scattering rates. The softening also reduces the transverse mode group velocities, which further

suppresses the thermal conductivity. Apparently, these factors act to cancel out the factors that would otherwise increase the thermal conductivity, as predicted for diamond and observed for ice [7] and MgO [10].

We measured a thermal conductivity of 34 W m^{-1} K^{-1} from an Al/Si sample decompressed from the primitive hexagonal Si-V phase near 16 GPa [Fig. 5(a), filled blue square]. Decompression of Si-V is known to yield polycrystalline metastable Si-III (BC8 structure) [77]. The measured Si-III thermal conductivity is comparable to that of our Si(Ge) with 0.9% Ge. Decompression from the β-Sn Si-II phase is also known to yield Si-III [77], but we measure a somewhat higher thermal conductivity of 72 W m^{-1} K^{-1} on recovery of Al-coated Si-II to ambient pressure [Fig. 5(a), filled blue triangle] [78]. This may be because decompressing from Si-II avoids the additional grain and defect formation that occurs when entering Si-V.

It is interesting to compare these Si-III thermal conductivities against those obtained in recent uniaxial high-pressure torsion experiments by Harish *et al.* [79]. In their experiment, two opposing anvils applied 24 GPa of pressure on single-crystalline Si wafers, and explored the resulting thermal conductivity as a function of torsion under pressure, before and after annealing at 600 °C. Our 72 W m^{-1} K^{-1} sample decompressed from Si-II has a similar thermal conductivity to that of samples by Harish *et al.* obtained from their zero torsion, post-anneal experiment. The 34 W m^{-1} K^{-1} sample released from 16 GPa Si-V likewise has a similar thermal conductivity to those of Harish *et al.*'s post-anneal samples after 10 revolutions of torsion at 24 uniaxial GPa. Evidently, entry into the Si-V phase by hydrostatic pressure reduces the thermal conductivity of recovered Si-III by a factor comparable to the effect of high-pressure torsion on Si post-anneal. For Harish *et al.*, the higher post-anneal thermal conductivities were attributed to three factors: thermal relaxation to Si-I, increased grain sizes, and reduced lattice defects. Since our samples were maintained at room temperature, it seems likely that the reduced thermal conductivity of our Si-III recovered from Si-V was due to grain and defect formation across the Si-II to Si-V phase transition.

VII. THERMAL CONDUCTIVITY—METALLIC

There was no visible roughening or grain formation across the diamond cubic to β-Sn transition. According to Shen *et al.* [76], the diamond cubic to β-Sn transition occurs by fast lattice fluctuations rather than static nucleation. However, the transition to primitive hexagonal Si is marked by simultaneous surface roughening and an abrupt increase in optical reflectivity. As shown in Fig. 5(a), between the diamond cubic and primitive hexagonal phases the Si and Si(Ge) thermal conductivities both increase sharply to similar values as the materials become metallic. Also, it is in the primitive hexagonal phase that we observe discrepancies between the thermal conductivities measured along orthogonal in-plane directions and in the [001] cross-plane direction of our samples, by beam offset and conventional TDTR, respectively.

Our beam offset data on bare metallic Si and Si(Ge) were taken along two perpendicular axes in the plane of the sample, so at each pressure point we have two beam offset data points, representing the in-plane thermal conductivities along two orthogonal axes. These are the diamond symbols in Fig. 5(b). The cyan and brown triangles are TDTR measurements on bare metallic Si and Si(Ge), respectively. We emphasize that TDTR on metallic samples without a transducer is not sensitive to the cross-plane thermal transport, but rather the in-plane thermal diffusivity, and then only if the lateral thermal penetration depth is a significant fraction of the laser spot size. Upward and rightward triangles are for increasing pressure, downward triangles for decreasing pressure. Overall the thermal conductivities for metallic Si and Si(Ge), including those using the Au(Pd) transducer, are consistently scattered within a band that increases with pressure up to the next phase transition near 36 GPa. The equivalence in Si and Si(Ge) metallic thermal conductivities within this band indicates that the phonon thermal conductivity, which should be strongly affected by the Ge defects in Si(Ge), is negligible compared to the electronic thermal conductivity in the metallic phase. This electronic dominance is typical for high thermal conductivity metals.

We were unable to measure bare Si or Si(Ge) above the *Cmca*/hcp transition, or to measure Au(Pd)-coated Si(Ge) on decompression from the hcp phase, because of excessive sample surface roughness. The large volume changes and grain nucleation across different Si phase transitions causes surface roughening that compounds with each transition. Excessive roughness prevents reliable TDTR measurement due to an excess of diffuse light scattering and thermoacoustic effects that distort the TDTR signal from the sample surface [44]. Our data for Au(Pd)-coated Si(Ge) above 36 GPa indicate a sharp loss in thermal conductivity in the mixed intermediate *Cmca*/hcp phase, followed by a rapid recovery into the hcp phase. Our measurements above 36 GPa for bare Si and Si(Ge) are suggestive of similar behavior, but are not reliable enough to report.

To properly understand the scattered band of thermal conductivities that we measure in the primitive hexagonal phase, we must revisit the geometry of the beam offset measurement and the symmetries involved in the semiconducting to metallic structural phase transitions in silicon. A conventional TDTR measurement, with or without a transducer, measures the temperature response of a sample due to radially symmetric heating at one point. Defining the plane of the sample as the *xy* plane, such a measurement can only sample the geometric mean thermal transport along the *x* and *y* in-plane axes.

Beam offset TDTR, however, breaks radial symmetry by displacing the probe beam relative to the pump. In beam offset the signal is the temperature profile along a line crossing the center of pump heat source. Over the time scale of the pump modulation frequency, an elliptical Gaussian temperature profile develops from the circular Gaussian pump heat source, due to the in-plane anisotropy of the sample. If the crystalline axes are known, two perpendicular beam offset line scans are sufficient to obtain the major and minor in-plane thermal conductivities [80].

We recall that the crystalline orientations of the diamond cubic, β-Sn, and primitive hexagonal phases are related to one another in a specific manner. The β-Sn tetragonal phase occurs as a 45° rotation about one of the cubic symmetry axes, for a threefold degeneracy in the orientations β-Sn can take relative

to the polished [001] Si face of our sample [76]. Either the β-Sn [001] is perpendicular to the polished surface, or the β-Sn [001] and [110] axes are parallel to that surface.

Next, the c axis of the primitive hexagonal phase forms along either the [100] or [010] axis of the β-Sn phase by a 90° rotation about the [010] or [100] axis, respectively [81,82]. Relating this back to our polished [001] diamond cubic surface, there are two scenarios. In the first scenario where the β-Sn c axis forms perpendicular to the sample surface, the primitive hexagonal c axis lies 45° out of the plane, along [011] and $[0\bar{1}\bar{1}]$, or $[01\bar{1}]$ and $[0\bar{1}1]$. Alternately, the hexagonal c axis lies in the sample plane, along [110], $[1\bar{1}0]$, [101], or $[10\bar{1}]$. In each scenario, the hexagonal ab plane cuts across one of the lateral or diagonal in-plane directions, respectively.

Due to how Si wafers cleave along the cubic symmetry axes, we know which orthogonal in-plane axes we measured by beam-offset TDTR. For bare Si and Si(Ge), we measured along the diagonal ([110], $[1\bar{1}0]$) and lateral ([100], [010]) in-plane axes of the diamond cubic phase, respectively. Finally, the conventional TDTR measurements in Fig. 5(a) on Au(Pd)-coated metallic Si and Si(Ge) were sensitive to the cross-plane thermal conductivity.

Since the primitive hexagonal phase has so much degeneracy in its choice of c axis, it is no surprise that the sample surface roughens on entering this phase. The samples become polycrystalline, and the scattered thermal conductivities imply significant anisotropy between the hexagonal ab-plane and c-axis thermal transport. However there is no clear trend to distinguish the beam offset and conventional data sets from bare Si and Si(Ge), so we do not know whether one or another set of orientations is preferred.

Regardless, we can say that the in-plane measurements had access to grain orientations varying from the hexagonal c axis to one of the planar hexagonal axes. The cross-plane data in Fig. 5(a), meanwhile, could conceivably probe orientations ranging from the c axis to 45° off the c axis. These ranges would be continuous for grain sizes smaller than the 3 μm e^{-2} radius laser spot for the bare Si, Si(Ge) measurements, or the 6 μm e^{-2} radius laser spot used on the Au(Pd)-coated samples.

If the c-axis thermal conductivity is higher than the in-plane thermal conductivity, as is typical for hexagonal metals, this may partly explain how the conventional TDTR measurements on Au(Pd)-coated Si and Si(Ge) [Fig. 5(a)] yielded above-average thermal conductivities within the range presented in the bare Si, Si(Ge) data [Fig. 5(b)]. That said, since the data sets in Figs. 5(a) and 5(b) have different sensitivities to the Si heat capacity C, that slight difference could just originate in a small systematic error in our calculated C.

We cannot simply take pairs of TDTR measurements with and without transducers in order to fit for C because the hexagonal metallic silicon is thermally anisotropic. Conventional TDTR with a transducer measures cross-plane thermal conductivity, TDTR without a transducer measures mean in-plane thermal conductivity, and beam offset TDTR measures two orthogonal in-plane thermal conductivities. All of these are different if the material is anisotropic. At best, we can only note the overlap in the thermal conductivity bands from the Au(Pd)-coated and bare metallic Si samples, and state that our *ab initio* silicon heat capacity is accurate to within the thermal anisotropy of the polycrystalline hexagonal metallic Si. But we cannot claim that it is experimentally verified to within less than the anisotropy of the sample.

VIII. ELECTRICAL RESISTIVITY

If we assume that the phonon contribution to the thermal conductivity of metallic Si and Si(Ge) is negligible, then we can take our analysis a step further by converting the electronic thermal conductivity Λ to an electrical resistivity ρ using the Wiedemann-Franz law, $\rho = L_0 T/\Lambda$, where $T \approx 300$ K is the temperature and L_0 is the Sommerfeld value of the Lorenz number $L_0 = 2.44\times10^{-8}$ W Ω K^{-2}. The result is shown in Fig. 6 for metallic Si and Si(Ge), in comparison to the ambient electrical resistivities of pure Al, Au, Zn, Cd, and Be [83,84]. The electrical resistivity in metallic Si and Si(Ge) is comparable to highly conductive metals such as Al and Au, with an electrical anisotropy of approximately 1.4, very similar to that of ambient hcp Be.

We compare our simple Wiedemann-Franz conversion to a more sophisticated electronic transport model to better understand the pressure dependence. In pure metals at room temperature, electron-phonon scattering controls the electrical resistivity. The Bloch-Grüneisen law gives the electrical resistivity due to electron-phonon scattering, with several assumptions. The assumptions include a spherical Fermi surface, no

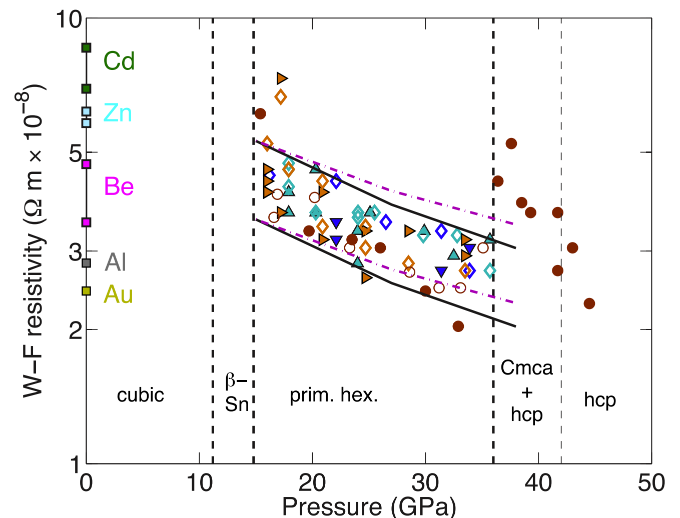

FIG. 6. (Color online) Wiedemann-Franz derived electrical resistivities. The Wiedemann-Franz law relates the electron-mediated thermal conductivity Λ_e to the electrical resistivity ρ of a metal according to $\Lambda_e = L_0 T/\rho$. Here T is the temperature and L_0 is the Sommerfeld value of the Lorenz number. We assume that the metallic thermal conductivities presented in Fig. 5(b) are equal to Λ_e. The resulting electrical resistivity for primitive hexagonal Si is comparable to that of highly conductive metals such as Al and Au, and very similar in magnitude and anisotropy (upper and lower bounds in data) to ambient Be, which is also a hexagonal metal. The symbols are the same as those in Fig. 5(b). The magenta dashed lines are upper and lower bound Bloch-Grüneisen models assuming purely anharmonicity-driven pressure dependence ($d \ln K/d \ln V \equiv \beta = 0$), and the black solid lines are the same, except $\beta = 1$ [Eqs. (1) and (2)].

resistivity from umklapp processes, and a Debye model for the phonon spectrum [85]. Because of the spherical Fermi surface, there are no normal electron-phonon processes for transverse phonons, leaving only N processes involving longitudinal acoustic phonons. None of these assumptions are strictly valid for Si, which becomes a tetravalent hexagonal metal under pressure. Umklapp processes in particular are known to be significant for other tetravalent metals, Sn and Pb [86].

Even so, we are encouraged by the work of Hanfland *et al.*, who measured the optical reflectivity of primitive hexagonal Si as a function of pressure, calculated the electronic band structure, and found their results consistent with Si being a nearly free electron metal in this phase [34]. Therefore we proceed with the Bloch-Grüneisen equation for the electrical resistivity:

$$\rho_{\mathrm{BG}} = \frac{K}{\Theta}\left(\frac{T}{\Theta}\right)^5 \int_0^{\Theta/T} \frac{z^5 e^z dz}{(e^z-1)^2}. \qquad (1)$$

Here K represents the combined factors relating to the Fermi surface geometry and electron-phonon scattering matrix elements, but which are assumed to be independent of temperature. The pressure dependence of $K = K_0(V/V_0)^\beta$, where $\beta \equiv d\ln K/d\ln V$, is generally not important unless the volume change causes the Fermi energy to cross an unpopulated band, which is not evident from Hanfland *et al.*'s band structure calculations [34]. The main part of the pressure dependence of the resistivity is expected to come from the lattice through the Debye temperature parameter Θ [85,87]. To calculate the pressure dependence of the Bloch-Grüneisen resistivity, we first formally differentiate Eq. (1):

$$\frac{d\ln\rho_{\mathrm{BG}}}{d\ln V} = \beta + 2\gamma. \qquad (2)$$

Note that $\gamma \equiv d\ln\Theta/d\ln V$ is the Grüneisen parameter. We then use our Wiedemann-Franz electrical resistivities to fit K_0 and β, and derive $\Theta \equiv (4/3)\langle E\rangle/k_{\mathrm{B}}$ from the first moment $\langle E\rangle$ of the same phonon densities of states that we calculated for the Si heat capacity. The frequencies corresponding to Θ across the primitive hexagonal phase are shown by vertical lines in Fig. 2. The resulting Θ varies from 505 to 607 K between 15 and 38 GPa, and γ is calculated from Θ and the Si equation of state.

Two Bloch-Grüneisen models are plotted in Fig. 6; the red line is for $\beta = 0$, and the black dot-dashed line is for $\beta = 1$. Much of the pressure dependence in our Wiedemann-Franz ρ can be explained by the pressure dependence of γ. Meanwhile we fit K_0 by the magnitudes of the upper and lower bounds of the measured ρ band near 15 GPa: $K_0 = 2.1\times10^4$ and $K_0 = 1.4\times10^4$ K $\mu\Omega$ cm, respectively. We notice that $\beta \approx 1$ is consistent with our pressure dependence, and that it is similar in magnitude to the β values of 0.87 and 0.78 for the other tetravalent metals, Pb and Sn [87].

IX. CONCLUSION

We have used conventional and beam-offset TDTR to establish the thermal conductivities of [001] Si and $Si_{0.991}Ge_{0.009}$ across the semiconductor-metal phase transition and up to 45 GPa. We performed measurements sensitive to alternately the thermal effusivity ΛC and the thermal diffusivity Λ/C, and obtained consistent fits for Λ with the same C that we derived from our *ab initio* phonon densities of states. The polycrystallinity of the primitive hexagonal Si phase, combined with our beam-offset TDTR technique, allowed us to measure the anisotropy in the thermal transport for hexagonal Si. We found that the metallic Si and Si(Ge) thermal conductivities are predominantly electronic in origin. Thus we applied the Wiedemann-Franz law to derive the associated electrical resistivity, and found it consistent with the Bloch-Grüneisen model.

ACKNOWLEDGMENTS

We thank Jay Bass and his students for use of their DAC facilities and for sharing their experience. This work was supported by the Carnegie-DoE Alliance Center (CDAC) Grant No. DE-FC52-29908NA28554, and was carried out in part in the Frederick Seitz Materials Research Laboratory Central Research Facilities, University of Illinois. Additional funding was provided by the U.S. Department of Energy National Energy Technology Laboratory under Award Number No. DE-EE0005976. Computations were performed on the Taub cluster maintained and operated by the Computational Science and Engineering Program at the University of Illinois.

[1] T. Lay, J. Hernlund, and B. A. Buffett, Nat. Geosci. **1**, 25 (2008).
[2] G. M. Manthilake, N. de Koker, D. J. Frost, and C. A. McCammon, Proc. Natl. Acad. Sci. USA **108**, 17901 (2011).
[3] W.-P. Hsieh, M. D. Losego, P. V. Braun, S. Shenogin, P. Keblinski, and D. G. Cahill, Phys. Rev. B **83**, 174205 (2011).
[4] Y. Xu, T. J. Shankland, S. Linhardt, D. C. Rubie, F. Langenhorst, and K. Klasinski, Phys. Earth Planet. Inter. **143-144**, 321 (2004).
[5] M. Osako, E. Ito, and A. Yoneda, Phys. Earth Planet. Inter. **143-144**, 311 (2004).
[6] M. Osako, A. Yoneda, and E. Ito, Phys. Earth Planet. Inter. **183**, 229 (2010).
[7] B. Chen, W.-P. Hsieh, D. G. Cahill, D. R. Trinkle, and J. Li, Phys. Rev. B **83**, 132301 (2011).
[8] T. Yagi, K. Ohta, K. Kobayashi, N. Taketoshi, K. Hirose, and T. Baba, Meas. Sci. Technol. **22**, 024011 (2011).
[9] K. Ohta, T. Yagi, N. Taketoshi, K. Hirose, T. Komabayashi, T. Baba, Y. Ohishi, and J. Hernlund, Earth Planet. Sci. Lett. **349-350**, 109 (2012).
[10] D. A. Dalton, W.-P. Hsieh, G. T. Hohensee, D. G. Cahill, and A. F. Goncharov, Sci. Rep. **3**, 2400 (2013).
[11] B. Lorenz and C. W. Chu, in *Frontiers in Superconducting Materials*, edited by A. V. Narlikar (Springer, New York, 2005), pp. 459–497.
[12] J. J. Hamlin Phys. C (Amsterdam, Neth.) (2015).
[13] J. R. Patterson, S. A. Catledge, Y. K. Vohra, J. Akella, and S. T. Weir, Phys. Rev. Lett. **85**, 5364 (2000).

[14] P. F. McMillan, M. Wilson, D. Daisenberger, and D. Machon, Nat. Mater. **4**, 680 (2005).
[15] R. P. Dias, C.-S. Yoo, M. Kim, and J. S. Tse, Phys. Rev. B **84**, 144104 (2011).
[16] R. P. Dias, C.-S. Yoo, V. V. Struzhkin, M. Kim, T. Muramatsu, T. Matsuoka, Y. Ohishi, and S. Sinogeikin, Proc. Natl. Acad. Sci. USA **110**, 11720 (2013).
[17] A. P. Nayak, S. Bhattacharyya, J. Zhu, J. Liu, X. Wu, T. Pandey, C. Jin, A. K. Singh, D. Akinwande, and J.-F. Lin, Nat. Commun. **5**, 3731 (2014).
[18] Z.-H. Chi, X.-M. Zhao, H. Zhang, A. F. Goncharov, S. S. Lobanov, T. Kagayama, M. Sakata, and X.-J. Chen, Phys. Rev. Lett. **113**, 036802 (2014).
[19] Y. Ding, C.-C. Chen, Q. Zeng, H.-S. Kim, M. J. Han, M. Balasubramanian, R. Gordon, F. Li, L. Bai, D. Popov, S. M. Heald, T. Gog, H.-k. Mao, and M. van Veenendaal, Phys. Rev. Lett. **112**, 056401 (2014).
[20] W.-P. Hsieh, M. Trigo, D. A. Reis, G. A. Artioli, L. Malavasi, and W. L. Mao, Appl. Phys. Lett. **104**, 021917 (2014).
[21] P. F. McMillan, Nat. Mater. **1**, 19 (2002).
[22] Y. S. Ju and K. E. Goodson, Appl. Phys. Lett. **74**, 3005 (1999).
[23] A. J. Minnich, J. A. Johnson, A. J. Schmidt, K. Esfarjani, M. S. Dresselhaus, K. A. Nelson, and G. Chen, Phys. Rev. Lett. **107**, 095901 (2011).
[24] J. A. Johnson, A. A. Maznev, J. Cuffe, J. K. Eliason, A. J. Minnich, T. Kehoe, C. M. S. Torres, G. Chen, and K. A. Nelson, Phys. Rev. Lett. **110**, 025901 (2013).
[25] R. B. Wilson and D. G. Cahill, Nat. Commun. **5**, 5075 (2014).
[26] T. Feng and X. Ruan, J. Nanomater. **2014**, 206370 (2014).
[27] M. I. McMahon, R. J. Nelmes, N. G. Wright, and D. R. Allan, Phys. Rev. B **50**, 739 (1994).
[28] M. Hanfland, U. Schwarz, K. Syassen, and K. Takemura, Phys. Rev. Lett. **82**, 1197 (1999).
[29] H. Olijnyk, S. Sikka, and W. Holzapfel, Phys. Lett. A **103**, 137 (1984).
[30] S. Minomura and H. Drickamer, J. Phys. Chem. Solids **23**, 451 (1962).
[31] F. P. Bundy, J. Chem. Phys. **41**, 3809 (1964).
[32] M. C. Gupta and A. L. Ruoff, J. Appl. Phys. **51**, 1072 (1980).
[33] K. J. Chang, M. M. Dacorogna, M. L. Cohen, J. M. Mignot, G. Chouteau, and G. Martinez, Phys. Rev. Lett. **54**, 2375 (1985).
[34] M. Hanfland, M. Alouani, K. Syassen, and N. E. Christensen, Phys. Rev. B **38**, 12864 (1988).
[35] C. Gao, Y. Han, Y. Ma, A. White, H. Liu, J. Luo, M. Li, C. He, A. Hao, X. Huang, Y. Pan, and G. Zou, Rev. Sci. Instrum. **76**, 083912 (2005).
[36] A. Jayaraman, Rev. Sci. Instrum. **57**, 1013 (1986).
[37] N. Velisavljevic, G. N. Chestnut, Y. K. Vohra, S. T. Weir, V. Malba, and J. Akella, Phys. Rev. B **65**, 172107 (2002).
[38] N. Velisavljevic, K. M. MacMinn, Y. K. Vohra, and S. T. Weir, Appl. Phys. Lett. **84**, 927 (2004).
[39] A. Kavner and C. Nugent, Rev. Sci. Instrum. **79**, 024902 (2008).
[40] Z. Du, G. Amulele, L. R. Benedetti, and K. K. M. Lee, Rev. Sci. Instrum. **84**, 075111 (2013).
[41] D. Zhang, J. M. Jackson, J. Zhao, W. Sturhahn, E. E. Alp, T. S. Toellner, and M. Y. Hu, Rev. Sci. Instrum. **86**, 013105 (2015).
[42] D. G. Cahill, Rev. Sci. Instrum. **75**, 5119 (2004).
[43] D. G. Cahill, W. K. Ford, K. E. Goodson, G. D. Mahan, A. Majumdar, H. J. Maris, R. Merlin, and S. R. Phillpot, J. Appl. Phys. **93**, 793 (2003).
[44] D. G. Cahill, P. V. Braun, G. Chen, D. R. Clarke, S. Fan, K. E. Goodson, P. Keblinski, W. P. King, G. D. Mahan, A. Majumdar, H. J. Maris, S. R. Phillpot, E. Pop, and L. Shi, Appl. Phys. Rev. **1**, 011305 (2014).
[45] W.-P. Hsieh, A. S. Lyons, E. Pop, P. Keblinski, and D. G. Cahill, Phys. Rev. B **84**, 184107 (2011).
[46] G. T. Hohensee, R. B. Wilson, and D. G. Cahill, Nat. Commun. **6**, 6578 (2015).
[47] G. T. Hohensee, W.-P. Hsieh, M. D. Losego, and D. G. Cahill, Rev. Sci. Instrum. **83**, 114902 (2012).
[48] J. P. Feser and D. G. Cahill, Rev. Sci. Instrum. **83**, 104901 (2012).
[49] D.-W. Oh, C. Ko, S. Ramanathan, and D. G. Cahill, Appl. Phys. Lett. **96**, 151906 (2010).
[50] S. K. Deb, M. Wilding, M. Somayazulu, and P. F. McMillan, Nature (London) **414**, 528 (2001).
[51] M. Rini, Z. Hao, R. W. Schoenlein, C. Giannetti, F. Parmigiani, S. Fourmaux, J. C. Kieffer, A. Fujimori, M. Onoda, S. Wall, and A. Cavalleri, Appl. Phys. Lett. **92**, 181904 (2008).
[52] W.-P. Hsieh and D. G. Cahill, J. Appl. Phys. **109**, 113520 (2011).
[53] Y. Shen, R. S. Kumar, M. Pravica, and M. F. Nicol, Rev. Sci. Instrum. **75**, 4450 (2004).
[54] H. K. Mao, J. Xu, and P. M. Bell, J. Geophys. Res.: Solid Earth **91**, 4673 (1986).
[55] A. D. Chijioke, A. Soldatov, and I. F. Silvera, J. Appl. Phys. **98**, 114905 (2005).
[56] A. Dewaele, J. H. Eggert, P. Loubeyre, and R. Le Toullec, Phys. Rev. B **67**, 094112 (2003).
[57] S. Klotz, J.-C. Chervin, P. Munsch, and G. L. Marchand, J. Phys. D: Appl. Phys. **42**, 075413 (2009).
[58] A. Schmidt, M. Chiesa, X. Chen, and G. Chen, Rev. Sci. Instrum. **79**, 064902 (2008).
[59] G. Kresse, J. Furthmüller, and J. Hafner, Europhys. Lett. **32**, 729 (1995).
[60] D. Alfè, G. D. Price, and M. J. Gillan, Phys. Rev. B **64**, 045123 (2001).
[61] G. Kresse and J. Furthmüller, Phys. Rev. B **54**, 11169 (1996).
[62] J. P. Perdew, K. Burke, and M. Ernzerhof, Phys. Rev. Lett. **77**, 3865 (1996).
[63] P. E. Blöchl, Phys. Rev. B **50**, 17953 (1994).
[64] G. Kresse and D. Joubert, Phys. Rev. B **59**, 1758 (1999).
[65] O. Jepsen and O. K. Andersen, Solid State Commun. **9**, 1763 (1971).
[66] G. Lehmann and M. Taut, Phys. Status Solidi B **54**, 469 (1972).
[67] P. E. Blöchl, O. Jepsen, and O. K. Andersen, Phys. Rev. B **49**, 16223 (1994).
[68] M. Methfessel and A. T. Paxton, Phys. Rev. B **40**, 3616 (1989).
[69] O. Sandberg and B. Sundqvist, J. Appl. Phys. **53**, 8751 (1982).
[70] T. Murakami, T. Hori, T. Shiga, and J. Shiomi, Appl. Phys. Express **7**, 121801 (2014).
[71] R. B. Wilson, B. A. Apgar, W.-P. Hsieh, L. W. Martin, and D. G. Cahill, Phys. Rev. B **91**, 115414 (2015).
[72] G. D. Mahan, Phys. Rev. B **79**, 075408 (2009).
[73] D. A. Broido, L. Lindsay, and A. Ward, Phys. Rev. B **86**, 115203 (2012).
[74] K. D. Parrish, A. Jain, J. M. Larkin, W. A. Saidi, and A. J. H. McGaughey, Phys. Rev. B **90**, 235201 (2014).
[75] T. Soma, Phys. Status Solidi B **99**, 701 (1980).

[76] G. Shen, D. Ikuta, S. Sinogeikin, Q. Li, Y. Zhang, and C. Chen, Phys. Rev. Lett. **109**, 205503 (2012).
[77] J. Z. Hu, L. D. Merkle, C. S. Menoni, and I. L. Spain, Phys. Rev. B **34**, 4679 (1986).
[78] J. M. Besson, E. H. Mokhtari, J. Gonzalez, and G. Weill, Phys. Rev. Lett. **59**, 473 (1987).
[79] S. Harish, M. Tabara, Y. Ikoma, Z. Horita, Y. Takata, D. Cahill, and M. Kohno, Nanoscale Res. Lett. **9**, 326 (2014).
[80] J. P. Feser, J. Liu, and D. G. Cahill, Rev. Sci. Instrum. **85**, 104903 (2014).
[81] S. M. Sharma and S. Sikka, J. Phys. Chem. Solids **46**, 477 (1985).
[82] R. J. Needs and R. M. Martin, Phys. Rev. B **30**, 5390 (1984).
[83] J. Bass, in *Metals: Electronic Transport Phenomena*, edited by K.-H. Hellwege and J. Olsen, Landolt-Börnstein, New Series, Group III, Vol. 15a (Springer, Berlin, 1982), Chap. 1.2.1, Pure Metal Resistivities at $T = 273.2$ K.
[84] B. A. Sanborn, P. B. Allen, and D. A. Papaconstantopoulos, Phys. Rev. B **40**, 6037 (1989).
[85] J. M. Ziman, *Electrons and Phonons: The Theory of Transport Phenomena in Solids* (Oxford University Press, New York, 2001).
[86] W. E. Lawrence and J. W. Wilkins, Phys. Rev. B **7**, 2317 (1973).
[87] A. Eiling and J. S. Schilling, J. Phys. F: Met. Phys. **11**, 623 (1981).
[88] J. L. Feldman and G. K. Horton, Phys. Rev. **137**, A1106 (1965).